Automotive Sheet Metal and Grid Digitizing Solutions

Allan D. Spence[1], H.-L. (Harley) Chan[2], J. Philip Mitchell[3] and David W. Capson[4]

[1]McMaster University, adspence@mcmaster.ca
[2]McMaster University, chanhl@mcmaster.ca
[3]McMaster University, mitchejp@mcmaster.ca
[4]McMaster University, capson@mcmaster.ca

ABSTRACT

Stamped automotive sheet metal parts must be measured for correct part shape, as well as for compliance to forming strain limits. Despite recent technological advances, use of non-contact, optical measurement techniques still has not replaced conventional touch probe and manual methods. This paper reports our recent laboratory experiences using two different non-contact solutions for sheet metal and grid digitizing. In the first solution, an electrochemically etched circle grid is first applied to the blank part. After forming, a CMM mounted triangulation laser digitizer measures the part coordinates and gray level. A parallel computer is used to accelerate data processing. The second solution begins with a square grid, and uses close-up passive stereo CCD cameras for digitizing. Both tailer-welded and constant thickness steel blanks are measured, and the resulting data is graphically presented in an easily interpreted format.

Keywords: strain analysis, laser digitizing, stereo vision, sheet metal stamping.

1. INTRODUCTION

To be acceptable, an automotive sheet metal part must: 1) have the correct geometric shape; and 2) remain within acceptable strain forming limits. An incorrect geometric shape results when the die shape is out of tolerance, or has not been corrected for material spring back. If excessive strain has occurred, the material may crack, buckle, or be too thin to meet in service strength requirements. Hence, during initial die tryout, as well as regularly during production, parts should be measured so that successful achievement of the above quality requirements can be confirmed. In conventional practice, the shape is digitized using a Coordinate Measuring Machine (CMM) equipped with a slow touch trigger probe. Strain is determined by electrochemically etching the part blank with a regular circle or square grid pattern, and then manually measuring the change in grid shape using a ruler and dividers or Mylar® tape.

Recent advances in sensor technology and computer processing speeds provide opportunities for substantial improvement over the prior practice. This paper reports our recent laboratory experiences in using both a laser triangulation digitizer and stereo Charge Coupled Device (CCD) cameras as sensors. A parallel computer is used to accelerate data processing for the circle grid, and the watershed algorithm is used to automate processing of the square grid. The remainder of the paper is organized as follows. In Section 2 automotive sheet metal stamping analysis requirements, including previous work, is reviewed. Section 3 describes the laser digitizer based solution. Section 4 describes the stereo CCD camera solution. A discussion and comparison of the two alternatives is contained in Section 5, followed by conclusions in Section 6.

2. SHEET METAL STAMPING ANALYSIS REQUIREMENTS AND PREVIOUS WORK

The shape of automotive sheet metal body panels is produced using a stamping die and press. As the die closes on the material, it experiences first elastic and then plastic deformation. When the die reopens, only the plastic component of the deformation is retained, and the relaxed elastic deformation results in the part returning to a shape that differs from the die. Although this elastic spring back can be estimated using numerical simulation, actual geometric measurement, and final modification of the die shape, is usually required to achieve the part design shape. Conventionally, these measurements are performed using a touch trigger probe (Fig. 1) equipped CMM, with an average data collection rate on the order of one point per second. The plastic deformation results in a permanent material strain, and, for acceptable parts, must be less than the material forming limit [9,16] (Fig. 2). That is, the strain achieved must be in

Fig. 1. Touch Trigger Probe Equipped CMM.

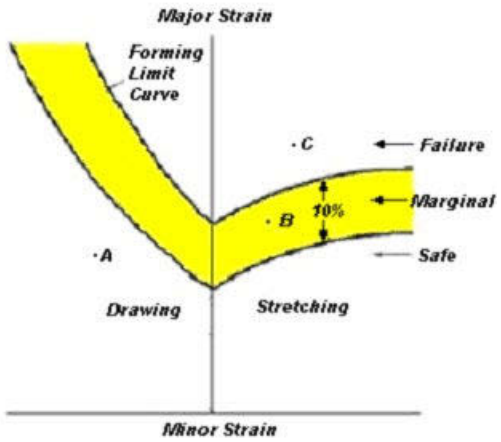

Fig. 2. Material Forming Limit Diagram and Curve [16].

region **A** below the Forming Limit Curve (FLC). Strain in region **B** is considered marginal, and strain in region **C** represents either fracture (in stretching) or wrinkling (in drawing) failure.

Experimentally, the strain is measured by electrochemically etching a dark circle or square grid on the undeformed material, forming it, and then manually measuring the change in shape using a ruler and dividers for square grids, or Mylar® tape for circle grids (Fig. 3) [4]. These conventional approaches are slow, tedious, and have low accuracy and repeatability. Typically they are performed only when conspicuous problems are observed, rather than as a regular process monitoring activity.

Recognizing the conventional approach limitations, a number of optical digitizer solutions for sheet metal and grid digitizing have been proposed. A number of laser digitizers are now commercially available, and are reviewed in [1]. Many of these have been adapted for use with CMMs that are commonly available at metal forming facilities. For strain analysis, single element systems use one CCD camera that is used to image a single grid element at a time (Fig. 4) [6]. The system is handheld and hence very portable. However, there is no correction for surface curvature, and the grid location on the part surface is not available. By taking images from two or more locations, stereo triangulation systems can simultaneously measure both the part geometry and the strain. Relatively accurate rotary table systems (Fig. 5) [25] move the part between images, but part volume is restricted to small laboratory sized specimens. Alternatively the part can remain stationary and the camera and tripod can be moved, but in this case accuracy is significantly reduced.

The research reported herein describes two practical sheet metal and grid digitizing solutions. The first solution exploits the capability of many CMM mounted laser digitizers to report, in addition to the 3-D part geometry coordinates, the surface reflected light intensity or gray level. Using a parallel computer to accelerate data processing speed, the gray level is automatically thresholded and used to separate the darker circle grid from the light metal background. Orthogonal data fitting is then used to determine the deformed circle axis lengths, and Forming Limit Diagrams (FLDs) as well as three dimensional colour thickness strain plots are prepared. The second solution uses a CMM mounted dual CCD camera sensor that can be articulated using a standard Renishaw plc PH10 probe head [20]. Vertices are triangulated to obtain the 3-D part geometry coordinates with no human intervention. Accurate strain plots are also prepared.

3. LASER DIGITIZER SOLUTION

For the laser digitizer solution, a circle grid was electrochemically etched onto the blank part. Circles were spaced on regular 3.175 mm centers, with a diameter of 2.54 mm. The circle circumference thickness was 0.254 mm. After forming, the part was measured using a Hymarc Hyscan 45C laser digitizer, mounted on a bridge style CMM (Fig. 6). This digitizer collects up to 1024 points per scan line, and at a rate of 3.3 scan lines per second. Over a small area, laboratory experience has determined a 1σ 3-D accuracy of approximately $10\ \mu$m . The gray level is simultaneously recorded with 12 bit resolution. By controlling the CMM speed and digitizer height above the part, points were collected at a nominal 0.1 mm square spacing.

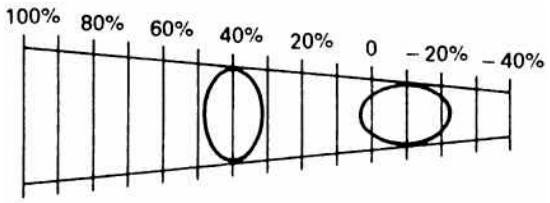

Fig. 3. Graduated Mylar® tape circle grid measurement [4].


Fig. 4. Handheld CCD camera grid measurement [6].

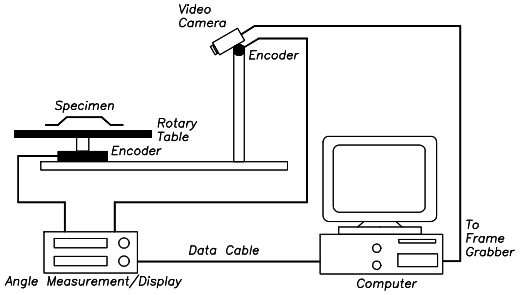

Fig. 5. Rotary table with fixed camera grid measurement [25].

Fig. 6. Laser digitizer sheet metal grid measurement.

3.1 Data Processing

Digitizer point data processing consisted of four procedures: 1) noise reduction; 2) thresholding; 3) grid element grouping; and 4) orthogonal least squares ellipse (deformed circle) fitting and strain calculation.

3.1.1 Noise Reduction

A survey of vision noise reduction algorithms is contained in [15]. For this work, a Gaussian filter was used, with a 3×3 pixel square mask. The mask component values were calculated using the formula

$$G(a,b)=c\cdot\exp\left(\frac{-\left(a^2+b^2\right)}{2\sigma^2}\right),\ \text{where the normalizing constant is}\ c=\left(\sum_{a=-1}^{1}\sum_{b=-1}^{1}\exp\left(\frac{-\left(a^2+b^2\right)}{2\sigma^2}\right)\right)^{-1}\ \text{and}\ \sigma=2 \qquad (1)$$

3.1.2 Thresholding

Thresholding is used to separate the dark coloured grid elements from the light coloured metal background. Because the part surface is generally not normal to the laser digitizer, the background intensity is highly variable (Fig. 7), making it difficult to distinguish from the grid. To address this problem, an adaptive technique was implemented based on previous research published by Yang and Yan [26], and is described below.

Let $g(x,y)$ be the intensity level at the centre pixel of a window f having size $(2\text{sw}+1)\times(2\text{sw}+1)$, where $\text{sw}=3$ is the circle circumference width in pixels. Based on the 8 neighbouring window pixels P_i, $i=0...7$, the current pixel is set to a value $b(x,y)$ using the following formula

$$b(x,y)=\begin{cases}1 & if\ \ \vee_{i=0}^{3}\left(B(P_i)\wedge B(P_{i+1})\wedge B(P_{i+4})\wedge B(P_{i+5})\right)\\ 0 & \text{otherwise}\end{cases} \qquad (2)$$

where $B(P_i)$ is a Boolean operation that is TRUE if $\text{ave}(P_i)-g(x,y)>T$, and FALSE otherwise. Pixels are labeled counterclockwise from the 3 o'clock position, $\vee$ denotes logical or, $\wedge$ denotes logical and, and subscript i arithmetic is modulo 8. The value for $\text{ave}(P_i)$ is calculated using the formula

$$\text{ave}(P_i)=\frac{\sum_{a=0}^{2\text{sw}}\sum_{b=0}^{2\text{sw}}P_i(a,b)}{(2\text{sw}+1)\times(2\text{sw}+1)} \qquad (3)$$

and the adaptive thresholding value T is calculated using the algorithm:

1) Calculate $f_{\max}=\text{MAX}(f)$, $f_{\min}=\text{MIN}(f)$ and $f_{\text{ave}}=\text{ave}(f)$

Fig. 7. Laser digitizer gray level.

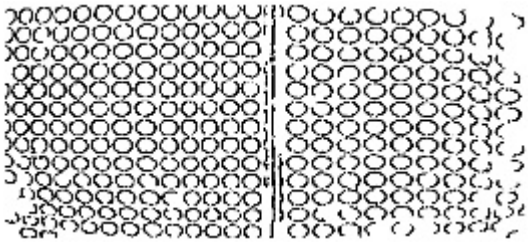

Fig. 8. Grid elements after grouping.

2) Calculate $|f_{max} - f_{ave}|$ and $|f_{min} - f_{ave}|$

3) If $|f_{max} - f_{ave}| < |f_{min} - f_{ave}|$, $T = \left(\frac{1}{3} f_{min} + \frac{2}{3} f_{ave}\right) \square \alpha$, if $|f_{max} - f_{ave}| < |f_{min} - f_{ave}|$, $T = \left(\frac{1}{3} f_{min} + \frac{2}{3} f_{ave}\right) \square \alpha$

4) If $|f_{max} - f_{ave}| = |f_{min} - f_{ave}|$, increase the window size to $(2sw+3) \times (2sw+3)$ and repeat from Step 1.
If $|f_{max} - f_{ave}| = |f_{min} - f_{ave}|$ again, $T = f_{ave} \square \alpha$.

The correction factor α is defined as

$$\alpha = \{1 \text{ if } f_{ave} < 90;\ \ 0.33 \text{ if } 90 \le f_{ave} < 130;\ \ 0.2 \text{ if } 130 \le f_{ave} < 170;\ \ 0.1 \text{ if } f_{ave} \ge 170\} \quad (4)$$

Sample results are shown in Fig. 8.

3.1.3 Grid Element Grouping

Points are next grouped into grid elements. For the circle grid, the shortest possible distance between two adjacent circumferences is 0.381 mm, and the distance between points within a single grid element is nominally 0.1 mm. Based on these observations, points were grouped together if they were separated by 0.3 mm or less. The group centre was then estimated by projecting the points onto an orthogonal least squares best fit plane, using a non-iterative algebraic ellipse fitting algorithm [12]. Groups with nearly identical centers were merged. After this step, any groups containing less than half of the 200 expected points were discarded.

3.1.4 Least Squares Ellipse Fitting and Strain Calculation

In order to perform strain analysis, the difference between the original circle diameter L_0, and the ellipse major L_1 and minor L_2 axis lengths, must be determined. Beginning with the algebraic fit from the previous step, a more accurate orthogonal least squares ellipse fit is obtained using the Orthogonal Distance Regression method [8]. The local surface curvature is used to correct the plane axis lengths back to the actual part surface.

The surface true strains are calculated using the formulae

$$\varepsilon_1 = \int_{L_0}^{L_1} \frac{dL}{L} = \ln\left(\frac{L_1}{L_0}\right);\ \ \varepsilon_2 = \int_{L_0}^{L_2} \frac{dL}{L} = \ln\left(\frac{L_2}{L_0}\right) \quad (5)$$

Because the total volume of the part does not change during the forming process, the third or thickness strain can then be calculated using the simple formula $\varepsilon_3 = -\varepsilon_1 - \varepsilon_2$. By creating a colour 3-D plot of this scalar quantity, a convenient interpretation of the forming severity can be obtained.

3.2 Parallel Computer Implementation

The processing algorithms described above were implemented using the standard Message Passing Interface (MPI) [11] on the Shared Hierarchical Academic Research Computer Network (SHARCnet) Compaq Alpha parallel computer [21]. Actual implementation uses a master/slave strategy in which the master process reads all image data, partitions it into equally sized slices, and transmits it, with specific processing instructions, to the individual slave process. The result of each slave process is sent back to the master process for merging.

3.3 Experimental Results

The procedures described above were experimentally carried out using a galvanized tailor welded steel blank. (Fig. 9). The left side undeformed thickness is 0.64 mm. The right side undeformed thickness is 1.14 mm. Approximately 6 million laser digitizer points were collected. A total of 900 ellipses, each containing approximately 200 points, were automatically thresholded, grouped, and fitted. Using the true thickness strain equation, a 3-D colour thickness plot

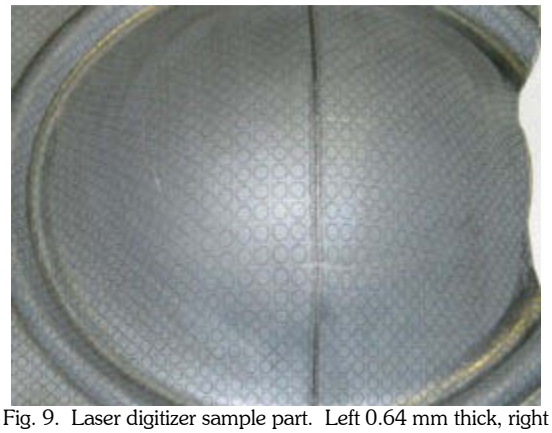

Fig. 9. Laser digitizer sample part. Left 0.64 mm thick, right 1.14 mm thick.

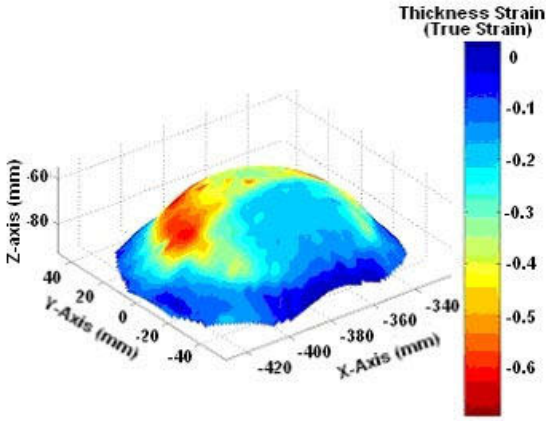

Fig. 10. Laser digitizer colour 3-D thickness plot.

was automatically created (Fig. 10). Such a plot, along with Forming Limit Diagrams (also automatically created), can be quickly interpreted and acted upon by manufacturing engineers. For serial processing, the elapsed computer processing time was 12 minutes. Using 7 parallel slave processors, this time was reduced to 2 minutes. Reported 1σ strain calculation accuracy for competing systems has been reported in the range of 2-5% [17]. Accuracy of the laser digitizer system depends on the location and orientation of the actual ellipse (circle) centre with respect to the nominal 0.1 mm sample spacing. Using mathematical simulation on a perfect grid image, the translation based uncertainty for a 2.54 mm diameter circle was 0.5 %. Using a 3 mm by 2.54 mm ellipse, the orientation uncertainty for each axis was found to be 0.9 %, and hence the combined ($k=1$) uncertainty is 1.1 % [14]. Imperfections in actual grids will increase this slightly, but, nonetheless, the laser digitizer solution compares very well to previous methods.

4. STEREO CCD CAMERA SOLUTION

The complete vision system is shown in Fig. 11 and consists of two Point Grey Dragonfly [19] 1024×768 8 bit gray level CCD board mount cameras attached to the CMM PH10 probe head that can be repeatably articulated in 7.5 degree pan or tilt steps. Each camera uses a 12 mm fixed focus Cosmicar/Pentax lens with an additional 1 mm lens spacer, and communicates with the data processing computer using the IEEE 1394 protocol. The mechanical mount provides electrical isolation from the CMM, yet includes a switch for latching the current CMM scale position. Overall mass is less than 300 g to avoid exceeding the PH10 torque limitations. Ambient room lighting, with an additional indirect incandescent light, was used for illumination.

4.1 Calibration

The camera calibration procedure is based on Zhang [27]. A 30 mm × 20 mm reference plane with a near perfect 2.54 mm pitch lithographically produced grid was used. The grid plane was oriented to 9 different positions, and was simultaneously imaged by both cameras. The grid line intersections (vertices) were detected and used to determine two Homogeneous Transformation Matrices (HTMs) that relate each Camera Coordinate Systems (CCS) to an overall sensor Stereo Coordinate System (SCS).

The cameras are translated by CMM axis motion, and rotated using the PH10 pan and tilt capability. Hence, the SCS point coordinates must be translated yet again into a Global Coordinate System (GCS) using registration. For any pair of PH10 poses, the registration transformation that accomplishes this consists of the rotation matrix $\mathbf{R}_{3\times3}$ and translation vector $\mathbf{T}_{3\times3}$ that minimizes

$$e^2(\mathbf{R},\mathbf{T}) = \frac{1}{n}\sum_{i=1}^{n}\left\|\mathbf{y}_i - (\mathbf{R}\mathbf{x}_i + \mathbf{T})\right\|^2 \tag{6}$$

where $\|\ \|$ is the usual Euclidean distance, the $\mathbf{x}_{i,3\times1}$ are the point coordinates in one pose, and the $\mathbf{y}_{i,3\times1}$ are the coordinates of the corresponding points in the second pose. A closed form solution using the Singular Value Decomposition (SVD) has been reported in [23]. Pennec's iterative mean shape method [18] was used to minimize the accumulated error for $N>2$ poses. Laboratory calibration was carried out using a 150 mm diameter dome shape part having the same lithographically produced grid described above.

Fig. 11. Stereo camera vision system.

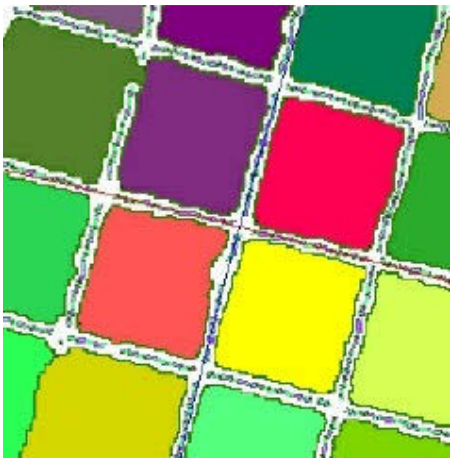

Fig. 12. Watershed algorithm [24] and parabola fitting.

4.2 Grid Intersection Detection

Grid intersection detection for the stereo CCD camera solution was implemented in 4 sequential steps: 1) noise reduction and gradient image calculation; 2) region segmentation and merging; 3) boundary processing; and 4) 3-D Reconstruction.

4.2.1 Noise Reduction and Gradient Image Calculation

As with the laser digitizer solution, the first image processing step was to remove high frequency noise using a Gaussian filter. To emphasize the grid edges, a 3×3 Sobel mask is then used.

4.2.2 Region Segmentation

To detect the grid intersection vertices, the images must be segmented into separate regions corresponding to each individual grid element. This task was attempted using both the watershed algorithm [24], and circular disk dilation [10] methods.

4.2.2.1 Watershed Algorithm Method

The watershed algorithm uses the image gray level as a measure of altitude. Conceptually, the algorithm can be visualized as filling a topological terrain with water. Region boundaries are constructed along the dikes that represent the highest altitudes remaining just prior to when the water would spill over and combine the regions. Because of varying image brightness, the regions will tend to be smaller than a complete grid square, and were therefore merged using the iterative algorithm described in [13] until their area is approximately 60 % of the grid square. Additional merging was performed if the resulting region compactness $C_{\text{region}} = \left(P_{\text{region}}^2 / A_{\text{region}} \right)$ (where P_{region} is the length of the region perimeter and A_{region} is the region area) is less than that of the two original regions. Representative results are shown in Fig. 12.

4.2.2.2 Circular Disk Dilation Method

The circular disk dilation method begins by removing small (<300 pixel), noisy areas (Fig. 13(a)), and then dilating the remaining boundaries outward using a circular disk (radius 15 pixels) (Fig. 13(b)). Circular disk erosion (radius 15 pixels) is then performed to restore the original boundaries, but with the effect of filling in small missing portions (Fig. 13(c)). Black/white complementing is then performed, and regions that are too small (<2000 pixels) or too large (>6500 pixels) are eliminated (Fig. 13(d)).

4.2.3 Boundary Processing

The remaining steps are illustrated using the Circular Disk Dilation method, but the steps are identical for the Watershed Algorithm method. After merging, the region boundaries are traversed with the highest curvature (k-curvature) being used to locate the 4 boundary points [15] (Fig. 13(e)). The centerline of the edge between regions, and between boundary points, is then computed using the Chamfer 3-4 distance metric [2] (Fig. 13(f)). Finally, the vertices of 4 adjacent regions are used to define a local coordinate system, and parabolas are then used to refine the vertex intersection coordinates to sub-pixel accuracy (Fig. 13(g,h)).

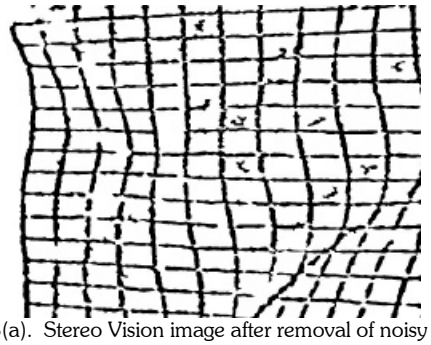

Fig. 13(a). Stereo Vision image after removal of noisy areas.

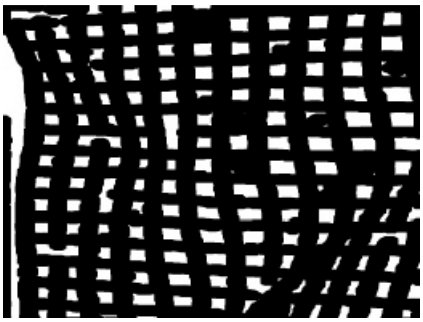

Fig. 13(b). Circular disk dilation.

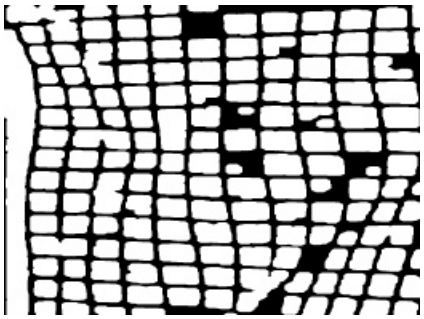

Fig. 13(c). Circular disk erosion.

Fig. 13(d). Black/white complementing and removal of too small/too large regions.

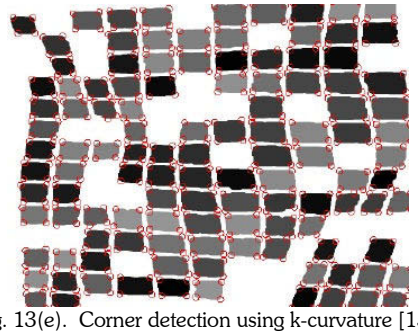

Fig. 13(e). Corner detection using k-curvature [15].

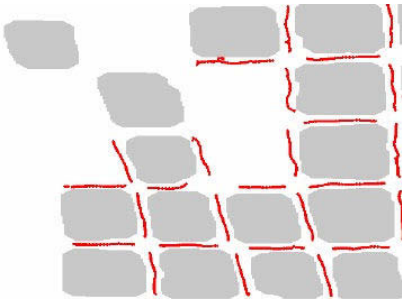

Fig. 13(f). Centerline calculation [2].

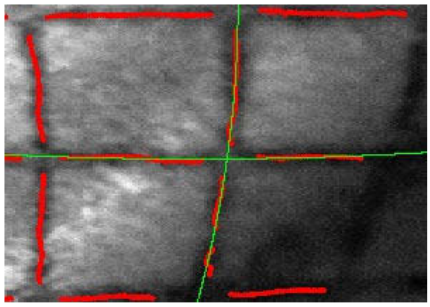

Fig. 13(g). Parabolic construction and intersection.

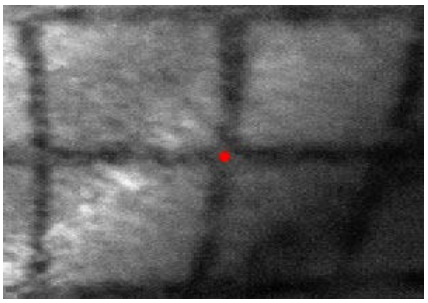

Fig. 13(h). Extracted intersection point.

4.2.4 3-D Reconstruction

After all of the above 2-D steps have been completed, vertices in the left and right images must be matched using triangulation to obtain the corresponding 3-D SCS vertex. Images are then rectified [7] to reduce the matching search space to one dimension. For the square grid, the ambiguous discrete and regular spacing of the vertices makes ordinary correlation based [15] selection of the correct match unreliable. To overcome this problem, image warping

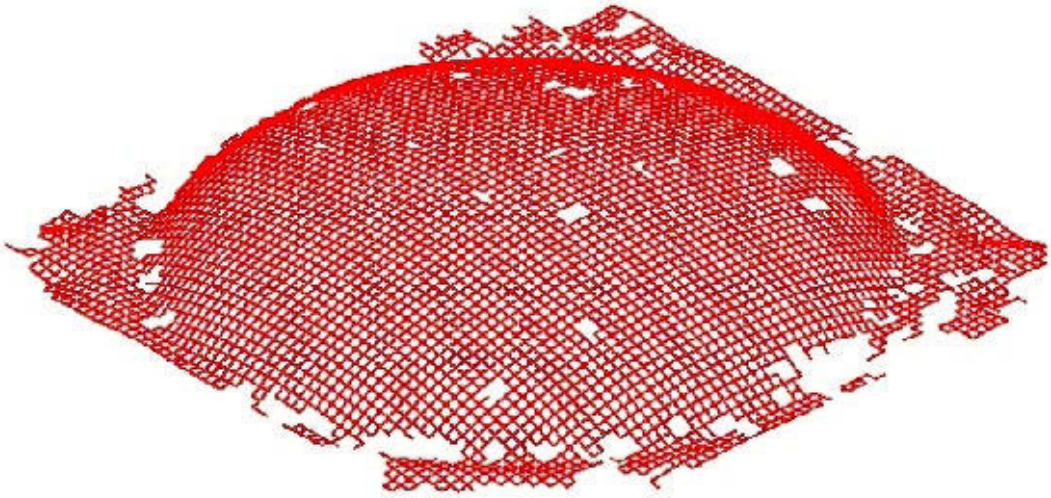

Fig. 14. 3-D stereo vision reconstructed grid plot.

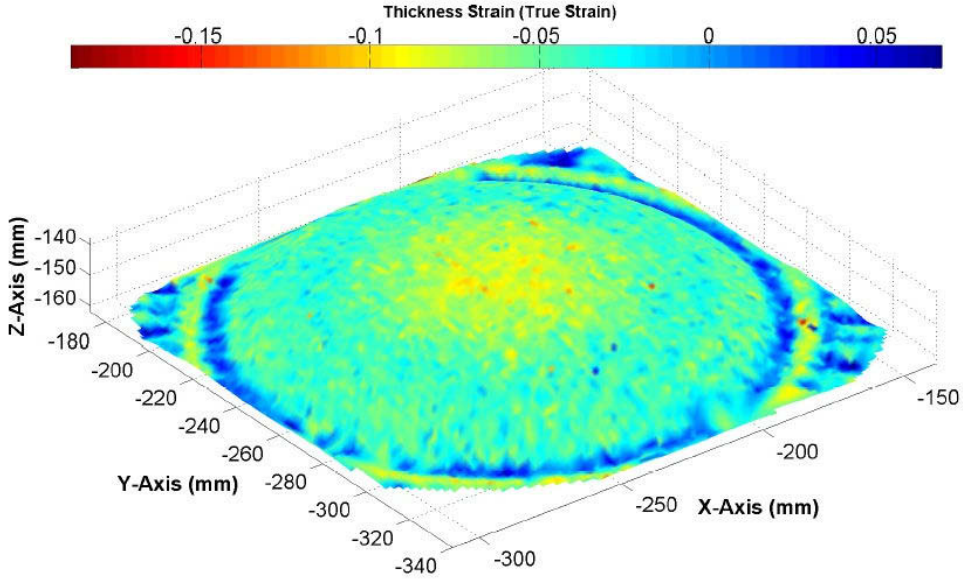

Fig. 15. 3-D stereo vision thickness strain plot.

[3] was used to estimate the vertex surface normals. Candidate point matches with significantly different normals were automatically discarded.

4.3 Strain Analysis

Strain analysis for the square grid can then be carried out using the procedure described in [22]. In short, each square is divided into 2 separate triangles, with a local coordinate system origin established at the middle vertex. On the undeformed sheet, the edge vertices will be located at coordinates (X_1, Y_1) and (X_2, Y_2). After forming, the middle vertex is maintained at the origin, and, applying a constant, second order tensor $\mathbf{F}_{2\times 2}$ to the edge vertices results in the linear systems

$$\begin{bmatrix} x_1 \\ y_1 \end{bmatrix} = \begin{bmatrix} F_{11} & F_{12} \\ F_{21} & F_{22} \end{bmatrix} \cdot \begin{bmatrix} X_1 \\ Y_1 \end{bmatrix}; \quad \begin{bmatrix} x_2 \\ y_2 \end{bmatrix} = \begin{bmatrix} F_{11} & F_{12} \\ F_{21} & F_{22} \end{bmatrix} \cdot \begin{bmatrix} X_2 \\ Y_2 \end{bmatrix} \tag{7}$$

where (x_1, y_1) and (x_2, y_2) are the deformed edge vertex coordinates. Rearranging

$$\begin{bmatrix} x_1 \\ x_2 \\ y_1 \\ y_2 \end{bmatrix} = \begin{bmatrix} X_1 & Y_1 & 0 & 0 \\ X_2 & Y_2 & 0 & 0 \\ 0 & 0 & X_1 & Y_1 \\ 0 & 0 & X_2 & Y_2 \end{bmatrix} \cdot \begin{bmatrix} F_{11} \\ F_{12} \\ F_{21} \\ F_{22} \end{bmatrix} \tag{8}$$

can now be solved for $\mathbf{F}$. The eigenvalues $\lambda_{1,2}$ of $\mathbf{F}$ can be computed using the Singular Value Decomposition (SVD), and satisfy the relationship $\varepsilon_{1,2} = \ln(\lambda_{1,2})$ where, as before, ε_1 and ε_2 are the surface true strains.

4.4 Experimental Results

The stereo CCD camera solution was tested on a steel sheet that was electrochemically etched with a 2.54 mm pitch square grid. In total 25 orientations of the PH10 probe head were used, and 170 separate stereo views of the part were captured. Using an Intel 1.6 GHz computer, approximately 19 hours was required for the Watershed Algorithm method, and 40 hours was required for the Circular Disk Dilation method. Over half of the time was spent on iterative orthogonal least square parabola fitting, and this is due to the very high resolution of pixels. To reduce processing time, the pixels could be thinned with an expected small effect on accuracy. A 3-D plot of the reconstructed grid, containing approximately 6,000 matched vertices, is shown in Fig. 14. After global registration, the maximum distance between corresponding points was less than 20 μm. Less than one minute of additional computer processing time was required for the strain analysis step, and the plotted results are shown in Fig. 15.

5. DISCUSSION

Sheet metal strain analysis is a problem that can significantly benefit from modern digitizing technologies. Because using Mylar® tape it is the easiest manual method, many companies continue to grid using circles. CMMs are also widely available at stamping facilities, and hence it was natural to consider this approach for the laser digitizer based solution. Through informal conversation, the authors have learned that many laser digitizers can provide gray level information, but this capability is not supported in commercial software. Our suggestion to vendors is to provide access to it so that third parties can further develop applications such as strain analysis. Even for regular geometric digitizing, the gray level provides additional feature information that can be exploited to improve accuracy.

One difficulty with laser digitizers is that they are line acquisition devices, and must be moved under computer control to acquire evenly spaced points. Motorized orthogonal axis CMMs support this, but installation on a manual portable arm CMM, such as a FARO [5], does not. For these devices, the stereo CCD camera solution, which records an area with each acquisition, is preferred. With suitable lens choices and a robust mounting enclosure, installation on a FARO arm or even an industrial robot would be very practical. These devices tend to have larger intrinsic geometric errors, and using the square grid vertex pattern makes it very easy to implement global registration. However, the high resolution laser digitizer curvature information is lost.

The large number of digitized points requires significant data processing times. For the laser digitizer solution this was improved by using parallel computing, and similar approaches, including optimized algorithm design, can be developed for the stereo CCD camera solution. Such improvements are necessary before online process control can be attempted. As well, it is recognized that representation and visualization, particularly including gray level, may be more appropriate using a polygon instead of a NURBS based modeler. Specular reflection from shiny metal surfaces is often an issue. For the work reported herein the steel was galvanized and this was not a significant problem. Polarizing filters, and careful control of ambient lighting for the stereo CCD camera solution, are topics for further research. For geometric digitizing applications other than strain analysis, structured light could also be used instead of etching a grid onto the part.

6. CONCLUSIONS

In this paper, two separate solutions for automotive sheet metal and grid digitizing were examined – one based on a laser digitizer, and one based on stereo CCD cameras. Both solutions were implemented on an orthogonal Coordinate Measuring Machine, and both methods achieved comparable accuracy. Although it is easier to manually measure circle grid, vertices of the square grid are more easily processed by computer. The large volume of data requires significant computer processing time, but it is expected that this can be significantly reduced through parallel processing and optimized algorithm design.

7. ACKNOWLEDGEMENTS

Equipment used for this research was purchased using a grant from the Canada Foundation for Innovation and Ontario Innovation Trust. Graduate student support was provided by a SHARCNET Ontario Research and Development Challenge Fund scholarship, Networks of Centres of Excellence – The Automobile of the 21st Century, and Natural Sciences and Engineering Research Council of Canada Individual Grants.

8. REFERENCES

[1] Blais, F., A Review of 20 Years of Range Sensor Development, *Videometrics VII - Proceedings of SPIE-IS&T Electronic Imaging*, SPIE, Vol. 5013, 2003, pp 62-76.

[2] Borgefors, G., Distance Transformations in Digital Images, *Computer Vision, Graphics and Image Processing*, Vol. 34, No. 3, 1986, pp. 344-371.

[3] Devernay, F. and Faugeras, D., Computing Differential Properties of 3-D Shapes from Stereoscopic Images without 3-D models, *Proc. of Computer Vision and Pattern Recognition,* 1994, pp. 208-213.

[4] Dinda, S., James, K.F., Keeler, S.P. and Stine, P.A., *How to Use Circle Grid Analysis for Die Tryout,* American Society for Metals, Metals Park, OH, 1981.

[5] FARO Technologies. Inc., Lake Mary, FL, www.faro.com.

[6] Forming Measurement Tool Innovations System Inc., *Grid Analyzer,* Hamilton, Canada, www.fmtisystems.com.

[7] Fusiello, A., Trucco, E. and Verri, A., A compact algorithm for rectification of stereo pairs, *Machine Vision and Applications,* Vol. 12, 2000, pp. 16-22.

[8] Gander, W., Golub, G.H. and Strebel, R., 1994, Least Squares Fitting of Circles and Ellipses, *BIT,* Vol. 34, 1994, pp 558-578.

[9] Goodwin, G.M., Application of Strain Analysis to Sheet Metal Forming Problems in the Press Shop, *La Metallurgica,* Vol. 60, 1968, pp 767-774.

[10] Gonzalez, R.C. and Woods, R.E., *Digital Image processing,* Addison-Wesley, Reading, Mass., 1992.

[11] Gropp, W., Lusk, E. and Skjellum, A., *Using MPI: Portable Parallel Programming with the Message-Passing Interface,* MIT Press, Cambridge, MA, 1994.

[12] Halír, R. and Flusser, J., Numerically Stable Direct Least Squares Fitting of Ellipses, *Proc. 6th Int. Conf. Central Europe Computer Graphics and Visualization*, WSCG'98, Plzeò, CZ, 1998, pp 125-132.

[13] Haris, K., Efstratiadis and S., Maglaveras, N., Hierarchical Image Segmentation Based On Contour Dynamics, *Proc. Int. Conference on Image Processing,* Oct. 7-10, Greece, 2001, pp 54-57.

[14] International Organization for Standardization, *Guide to the Expression of Uncertainty in Measurement,* Geneva, Switzerland, 1995.

[15] Jain, R., Kasturi, R. and Schunck, G., 1995, *Machine Vision*, McGraw-Hill, New York, NY, 1995.

[16] Keeler, S.P., *Training Manual - Enhanced FLC Project,* The Auto/Steel Partnership, Southfield, MI, http://www.a-sp.org/.

[17] Manthey, D.W. and Bassette, R.M. and Lee, D., 1993, Comparison of Different Surface Strain Measurement Techniques Used for Stamped Sheet Metal Parts, *Proc. Int. Body Engineering Conference: Body Assembly & Manufacturing*, Sept. 21-23, Detroit, MI, 1993, pp 106-111.

[18] Pennec, X., Multiple registration and mean rigid shapes: Application to the 3D case, *16th Leeds Annual Statistical Workshop*, Leeds, U.K., 1996, pp 178–185.

[19] Point Grey Research Inc., Vancouver, BC, www.ptgrey.com.

[20] Renishaw plc, *PH10M Probe Head,* UK, www.renishaw.com.

[21] Shared Hierarchical Academic Research Computer Network, www.sharcnet.mcmaster.ca.

[22] Sowerby, R., Duncan, J.L. and Chu, E., The Modelling of Sheet Metal Stampings, *Int. J. Mechanical Sciences,* Vol. A28, No. 7, 1986, pp 415-430.

[23] Umeyama, S., Least-Squares Estimation of Transformation Parameters Between Two Point Patterns, *IEEE Trans. Pattern Analysis And Machine Intelligence*, Vol. 13, No. 4, 1991, pp 376-380.

[24] Vincent, L. and Soille, P., Watersheds in digital spaces: An efficient algorithm based on immersion simulations, *IEEE PAMI,* Vol. 13, No. 6, 1991, pp 583-598.

[25] Vogel, J.H. and Lee, D., The Automated Measurement of Strains from Three-Dimensional Deformed Surfaces, *Journal of Metals,* Vol. 42, 1990, pp 8-13.

[26] Yang, Y. and Yan, H., 2000, An Adaptive Logical Method for Binarization of Degraded Document Images, *Pattern Recognition,* Vol. 33, 2000, pp 787-807.

[27] Zhang, Z., A Flexible New Technique for Camera Calibration, *IEEE Trans. Pattern Analysis And Machine Intelligence,* Vol. 22, No. 11, 2000, pp 1330-1331.